The Au-substituted Al - Cu - Fe icosahedral phase: evidence for bond hybridization

The Au-substituted Al–Cu–Fe icosahedral phase: evidence for bond hybridization

R Popescu†, D Macovei†, M Manciu†, F Zavaliche†, D Fratiloiu†,
A Jianu†, A Devenyi†, R Manaila†, Y Xie‡, T Hu‡, B R Orton§,
R J Cernik‖ and C C Tang‖

† Institute of Physics and Technology of Materials, PO Box MG-7, Bucharest-Magurele, RO-76900, Romania
‡ Institute of High Energy Physics, Beijing Synchrotron Radiation Facility, Beijing, People's Republic of China
§ Physics Department, Brunel University, Uxbridge, Middlesex UB8 3BH, UK
‖ Daresbury Laboratory, Warrington WA4 4AD, UK

Abstract. Au-substituted Al–Cu–Fe icosahedral phases, $Al_{62}Cu_{25.5-x}Au_xFe_{12.5}$ ($x \leqslant 7$), were prepared by melt spinning. EDS data showed that Cu as well as Al atoms are effectively substituted for with Au. The hypercubic lattice parameter of as-quenched samples slowly increases with x, while phonon- and phason-type disorders are not affected by Au substitution. Experimental structure factors for 'sum' lines were used to derive an average radius of the atomic hypersurfaces.

Comparison of experimental versus calculated ratios of structure factors for different models yielded information about the Au distribution over the icosahedral sites. It was inferred that a fraction of the gold shapes its Al surrounding in a $AuAl_2$-type configuration. Evidence was found for d–sp hybridization of Au–Al bonds, on the basis of the 'white-line' area at the Au L_3 absorption edge.

1. Introduction

Investigation of the stable Al–Cu–Fe icosahedral (i-) phase has quickly progressed, due to the possibility of growing relatively large quasicrystals [1, 2]. Its stability zone in the ternary phase diagram was also reported: a small region, centred on the composition $Al_{62}Cu_{25.5}Fe_{12.5}$, corresponds to an i-phase stable up to the melting point [3]. Slight changes in alloy composition (less than 1 at.%) were shown [4] to induce a transition of the i-phase to a stable rhombohedral approximant at around 700 °C. Much less is known about the structure and stability of quaternary i-phases, derived from i-Al–Cu–Fe by substitution for the key element Cu. The latter is considered to be a stabilizing component in i-Al–Cu–Fe, due to the low density of d states contributed at the Fermi level E_F [5], thereby enhancing the Hume-Rothery character of the alloy. Substitution for Cu with isoelectronic noble metals (Au, Ag) could therefore influence the stability of the icosahedral network and modify its compositional range.

On the other hand, Au is known to develop strongly sp–d hybridized bonds with less electronegative elements like Al [6, 7]. As Al is the prevailing element in the Al–Cu–Fe phases, we expect sp–d hybrid bonds to form between substituted Au and Al neighbours in its first coordination sphere. Therefore, establishing a new set of Au–Al hybrid bonds

could influence the energetical stability of the i-phase. Structural changes are also expected to result from this substitution, concerning bond lengths and phason/phonon disorder. This paper aims at finding structural evidence for bond hybridization induced via noble-metal substitution, using x-ray diffraction and XANES spectroscopy.

Au-substituted i-AlCuFe phases were investigated in the as-quenched state. Therefore, part of the phonon/phason disorder is to be attributed to the quenching process. We will however be interested in substitution-induced disorder only, assuming the quenched-in contribution to be relatively constant at different compositions. Efforts towards obtaining more perfect samples by annealing must be preceded by a careful study of the quaternary equilibrium phase diagram, at different temperatures.

Most of the actual research on quasicrystals is focused on 'perfect' samples, with vanishing structural disorder in narrow compositional ranges. We cannot expect to obtain 'perfect' as-quenched icosahedral phases in broad quaternary composition zones. Despite this fact, much is to be learned from their structural study, especially as regards chemical bonding and the local configurations.

2. Experimental procedure

2.1. Sample preparation

Substituted $Al_{62}Cu_{25.5-x}Au_xFe_{12.5}$ samples ($x = 1, 2, 5,$ and 7) were prepared by melt spinning. Primary alloys are obtained in an arc furnace from elements with 99.99% purity. Pieces of primary alloys were induction melted in the quartz crucible of a melt-spinning installation in Ar atmosphere, and rapidly quenched ribbons (thickness 20–25 μm) were obtained at a cooling wheel speed of 1700 rotations per minute (linear speed 35 m s^{-1}). Details about the preparation and measurements of the Ag-substituted samples, which will be used for comparison, are given in [8].

2.2. X-ray diffraction, XANES, and microstructure

XRD experiments for samples with $x = 2, 5,$ and 7 were conducted at the SRS Daresbury (UK) Station 2.3, using synchrotron radiation ($\lambda_n = 1.50$ Å). Diffraction data were also taken with wavelengths of 1.0402 Å (λ_{Au}) and 1.3808 Å (λ_{Cu}), lying at the inflexion points of the Au L_3 and Cu K absorption edges, respectively.

Additional diffracted intensity data for $x = 0$ and 1 were collected on a θ–2θ diffractometer, using Cu Kα radiation and a graphite monochromator placed before the NaI scintillation detector. The instrumental FWHM was determined with a standard, poly-Si sample and interpolated for particular 2θ-angles. It ranged from 5×10^{-4} Å^{-1} to 8×10^{-4} Å^{-1} in units of k ($k = 2(\sin\theta)/\lambda$) over the angular domain investigated. The line profiles were measured in steps of $\Delta(2\theta) = 0.01$. Rachinger doublet corrections were applied, and the instrumental width was subtracted using an adequate formula for intermediate Gauss–Cauchy profiles:

$$B^2 = (B_0 - b)(B_0^2 - b^2)^{1/2}$$

where B_0 and b stand for the raw and instrumental widths, respectively. The lattice parameters were derived by a Cohen–Wagner extrapolation procedure, mostly versus $\cot^2\theta$ and $\cos\theta\cot\theta$, which yielded the best linear correlation of instrumental errors on line positions.

The XANES spectra of the i-$Al_{62}Cu_{25.5-x}Au_xFe_{12.5}$ samples at the Au L_3 edge were recorded in the fluorescence mode at the Beijing Synchrotron Radiation Facility (BSRF),

beamline 4W1B, with an electron energy of 2.2 GeV, and the storage ring current in the range 40–60 mA. The incident x-ray beam was analysed with a Si(111) double-crystal monochromator. Higher harmonics in the diffracted beam were removed by a slight detuning of the second crystal of the monochromator. The experiments were performed at room temperature.

Microstructure investigations were conducted on a Philips SEM 515 instrument with EDS facilities.

Table 1. EDS compositions of the icosahedral phase in $Al_{62}C_{25.5-x}Au_xFe_{12.5}$ as-quenched ribbons.

| x (at.%)	Al (at.%)	Cu (at.%)	Fe (at.%)	Au (at.%)	Atoms substituted for with Au
1	59.6	26.0	13.4	1.0	1 Au → 1 Al[a]
2	60.6	25.1	12.2	2.1	1 Au → 1 Al; 1 Au → 1 Cu
5	59.6	22.3	12.6	5.5	2 Au → 2 Al; 3 Au → 3 Cu
7	63.5	18.1	11.6	6.8	7 Au → 7 Cu

[a] → stands for 'is substituted for'.

3. Microstructure

SEM investigations showed large ($\sim$5 μm) rosette-like formations, characteristic for i-phases, with a central Al-rich tip. Local composition data were taken in the SEM mode on the rosette arms (table 1). The area investigated was 20 nm in diameter. Extending it to a 20 μm size on a particularly large grain changed the results by less than 1 at.%, i.e. within the accuracy of the local composition data. Table 1 shows that the icosahedral phase composition closely follows the global Au content x. Changes in Al and Cu concentrations can be used to assess the actual atoms which are substituted for with Au (rounded-up figures are given in table 1). As can be seen, Au takes the place of both Al and Cu, with a preference for the latter. The atom substitutions shown in table 1 should only be taken in a statistical sense, as a general preference of Au for certain sites. This preference cannot be expected to depend markedly on the Au content for the small concentration range investigated. Therefore an averaged site preference, taken over the four compositions in table 1, is considered to be more meaningful. In a study of Ag-substituted i-AlCuFe [8], the same type of (Al + Cu) mixed replacement was found, but with an enhanced preference of Ag for Al sites.

4. Phase composition

Diffraction patterns (figure 1) show a dominant icosahedral phase and a minor crystalline one. The latter is of the β-FeAl type (CsCl structure). Positions of three accessible lines of the β-phase yielded a lattice parameter $a = 2.57 \pm 0.01$ Å for samples with $x = 1$ and 5, as compared to $a = 2.90$ Å for β-FeAl. The difference suggests a more complex composition of the β-phase, as is also reported for Ag-substituted i-AlCuFe [8]. The ratio between the integrated intensities $\beta(110)/i(18, 29)$ (the most intense lines of both phases), shows no consistent trend with x. This is to be contrasted with the case for the Ag-substituted alloys [8], where the ratio between crystalline β- and icosahedral fractions steadily increases with x. Failure to eliminate the crystalline phase by annealing in the latter system led to the
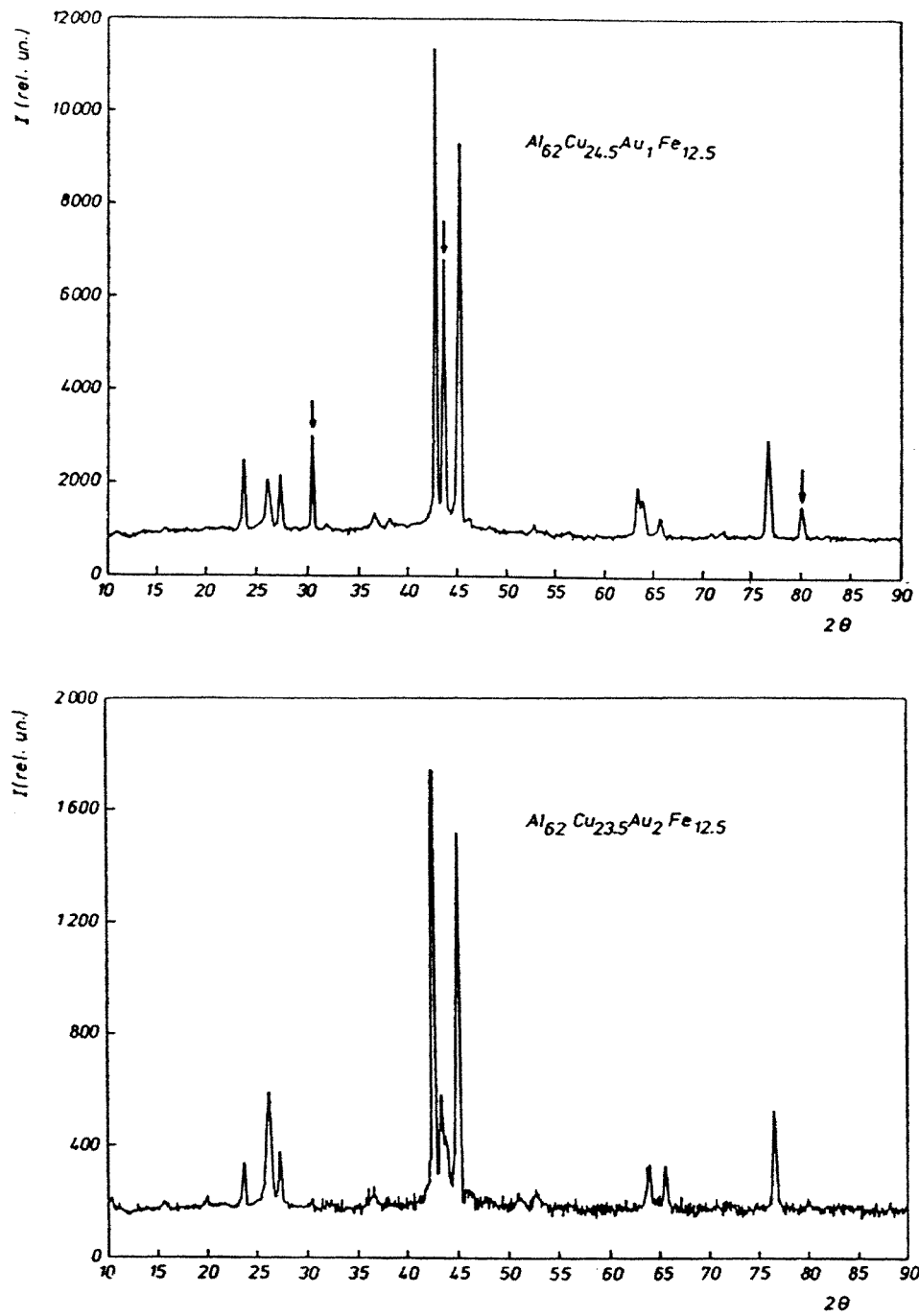
Figure 1. Diffraction patterns of $Al_{62}Cu_{25.5-x}Au_xFe_{12.5}$ as-quenched ribbons (Cu Kα). Arrows: lines belonging to the crystalline cubic β-phase; crossed arrows: AuAl$_2$-type details. As-prepared compositions are indicated.
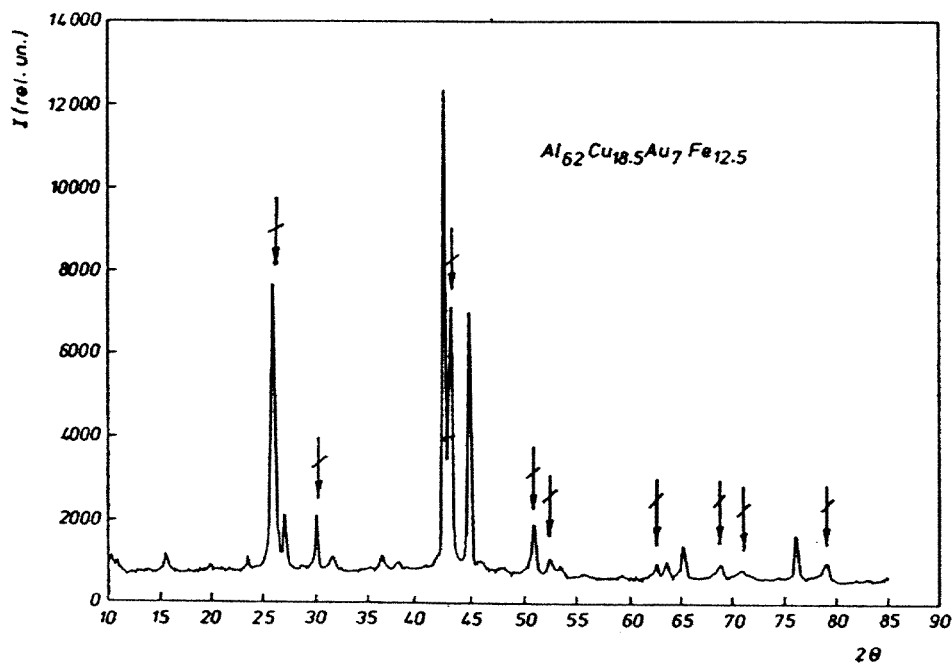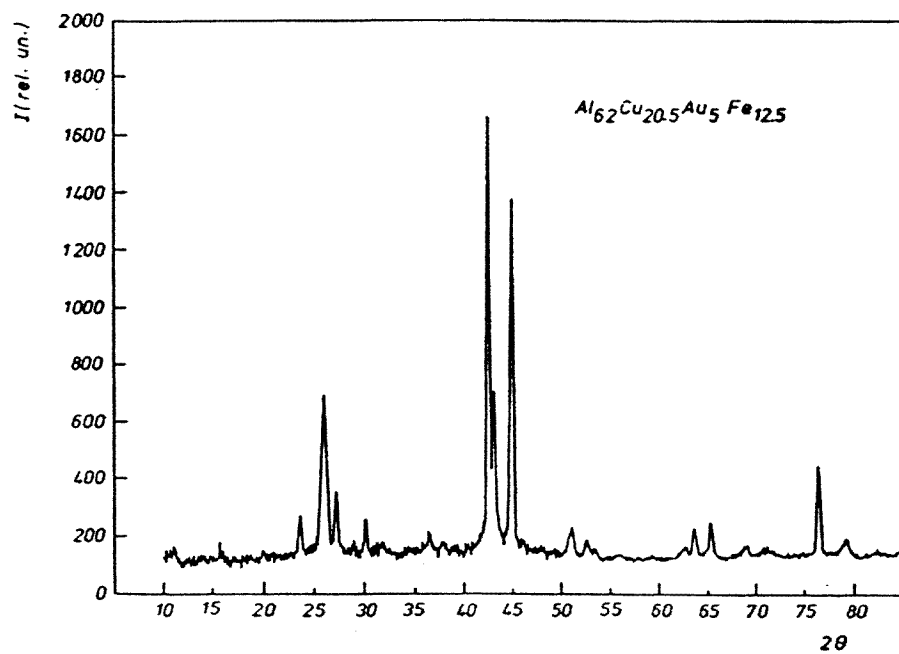
Figure 1. (Continued)

conclusion that the region of the AlCuFeAg compositions investigated is biphasic up to the melting point [8]. For $x = 5$ and 7, weak diffraction details appear (figure 1) corresponding to lines of the AuAl$_2$ cubic compound (CaF$_2$-type). They will be commented on in the following.

5. The location of Au in the icosahedral network

5.1. Atomic sites in i-AlCuFe

Recent models were devised for the i-Al$_{63}$Cu$_{25}$Fe$_{12}$ phase [9, 10], based upon neutron diffraction experiments [2]. These models correctly account for the intensities diffracted by a 'perfect' Al$_{63}$Cu$_{25}$Fe$_{12}$ quasicrystal, grown at 860 °C from a partially molten alloy [2].

According to the models, the 6D cubic lattice (type F, parameter 2Z) comprises four types of site, occupied by 3D atomic surfaces (quasi-atoms): N$_1$ (cell corners), N$_2$ (half-edges), BC$_1$, and BC$_2$ (body-centre positions in the Z-edge cell). Each atomic surface has full icosahedral symmetry and a triacontahedron-related shape. Their occupation can be statistically defined [2] as

$$
\begin{aligned}
&\text{N}_1\text{: Al (possibly also some Fe atoms [10])}\\
&\text{N}_2\text{: 50\% Cu} + 32\% \text{ Fe} + 18\% \text{ Al}\\
&\text{BC}_1\text{: Cu}\\
&\text{BC}_2\text{: empty}
\end{aligned}
\tag{1}
$$

for the composition and sample history mentioned above. The atomic surfaces are confined in the complementary $E_\perp$-space. They project onto the real $E_\parallel$-space as centres of clusters, comprised of concentric atomic shells.

5.2. Structure factors for i-Al–Cu–Fe diffraction lines

The structure factor $F(G)$ for an icosahedral diffraction peak can be written as a sum of contributions $F_j(G)$, due to the different atomic surfaces j:

$$
F_j(G) = \mu_j \tilde{f}_j(G_\parallel) \exp(2\pi \mathrm{i} G \cdot u_j) \int_{\Sigma_j} \exp(2\pi \mathrm{i} G_\perp \cdot u_\perp)\, \mathrm{d}u_\perp
\tag{2}
$$

where $\mu_j =$ the multiplicity of the j-sites, located at u_j in 6D space, $G = G_\parallel + G_\perp$ is the 6D reciprocal vector, and $\tilde{f}_j(G_\parallel)$ is the atomic scattering amplitude, averaged over the species populating the hypersurface Σ_j. The integral in equation (2) represents the Fourier transform $S_j(G_\perp)$ of the atomic hypersurface Σ_j. For $G_\perp \to 0$, the integral $S_j(G_\perp)$ converges towards the volume V_j of the atomic hypersurface.

Using the u_j-coordinates of sites N$_1$, N$_2$, BC$_1$, and BC$_2$, the structure factors of different icosahedral reflections fall (for $G_\perp \to 0$) into four classes [2], corresponding to four sets of phases $2\pi \mathrm{i} G \cdot u_j$ and to different combinations of Cahn indices:

$$
\begin{aligned}
F_a &= |F_{\text{N}_1} + F_{\text{N}_2} + F_{\text{BC}_1} + F_{\text{BC}_2}| && \text{for } N, M \text{ even;}\\
F_b &= |F_{\text{N}_1} + F_{\text{N}_2} - F_{\text{BC}_1} - F_{\text{BC}_2}| && \text{for } N \text{ even, } M \text{ odd;}\\
F_c &= |F_{\text{N}_1} - F_{\text{N}_2} - F_{\text{BC}_1} + F_{\text{BC}_2}| && \text{for } N, M \text{ odd;}\\
F_d &= |F_{\text{N}_1} - F_{\text{N}_2} + F_{\text{BC}_1} - F_{\text{BC}_2}| && \text{for } N \text{ odd, } M \text{ even.}
\end{aligned}
\tag{3}
$$

Lines of types c and d are determined by an F-type superstructure superposed on lines of types a and b.

The product $\tilde{\mu}_j = \mu_j V_j$ is proportional to the number of atoms actually occupying the hypersurface Σ_j, which contributes the scattering amplitude F_j. The effective multiplicities $\tilde{\mu}_j$ of sites N_1, N_2, BC_1 were estimated on the basis of the occupancies (1) ($\sum_j \tilde{\mu}_j = 100$):

$$\tilde{\mu}_{N_1} + 0.18\tilde{\mu}_{N_2} = 63 \text{ Al atoms}$$
$$\tilde{\mu}_{BC_1} + 0.5\tilde{\mu}_{N_2} = 25 \text{ Cu atoms} \tag{4}$$
$$0.32\tilde{\mu}_{N_2} = 12 \text{ Fe atoms.}$$

Solving the system (4) yields $\tilde{\mu}_{N_1} = 56.25$, $\tilde{\mu}_{N_2} = 37.5$, and $\tilde{\mu}_{BC_1} = 6.25$. These values can be used to calculate the contribution of sites N_1, N_2, and BC_1 to the structure factors in equations (3). In the limit $G_\perp \to 0$,

$$|F_j|(G_\parallel) = \tilde{\mu}_j \tilde{f}_j(G_\parallel) = \tilde{\mu}_j \sum_i c_i^j f_i(G_\parallel) \tag{5}$$

where $j = N_1$, N_2, BC_1, and i runs over the atomic species with x-ray scattering amplitudes f_i, occupying sites j in the concentration c_i^j ($\sum_i c_i^j = 1$). BC_2 sites were considered empty in Au-substituted samples, as for i-Al–Cu–Fe.

5.3. Form factors of atomic hypersurfaces

The hypersurfaces Σ_j have triacontahedral shapes and can be considered as quasi-spherical, deviations from a true sphere becoming apparent in the Fourier transforms at large $G_\perp$-values only. Therefore, in the relatively low-$G_\perp$ domain investigated ($G_\perp \leqslant 7.2 \times 10^{-2}$ Å^{-1}), a classical spherical form factor can be used to approximate the $S_j(G_\perp)$ (and $F_j(G_\perp)$) trend [11]:

$$S_j(G_\perp) \propto \left[\frac{\sin(2\pi G_\perp R_c)}{(2\pi G_\perp R_c)^3} - \frac{\cos(2\pi G_\perp R_c)}{(2\pi G_\perp R_c)^2} \right]. \tag{6}$$

Here, R_c stands for the radius of the sphere in the $E_\perp$-space which best approximates the actual hypersurface.

The experimental structure factors $F(G_\perp)$ for lines a–d (equations (2) and (3)) could in principle be used to derive R_c-values for the sites N_1, N_2, and BC_1. Careful analysis of low-$G_\perp$ data for the four line types (a–d) allowed to infer a multiple-shell structure of hypersurfaces in the i-AlPdMn phase [12]. However, in our case, having four atomic species present in varied concentrations, a similar goal would be too ambitious. We used instead the experimental structure factors $F_k(G_\perp)$ ($k = a, b$), and their approximation by equation (6) to estimate global R_c-values, averaged over all icosahedral sites. Of course, atomic surfaces occupied by the strong scatterers (e.g. Au) will prevail in this average.

Figure 2 shows the experimental $F_a(G_\perp)$ dependences for Au-substituted samples. A Debye–Waller correction $\exp(-(B/4)G_\parallel^2)$ improves the fit to a spherical form factor (equation (6)). The values of the resulting parameter R_c are listed in table 2 for different radiations. R_c^{Au} and R_c^{Cu} are slightly different from R_c^n, for the compositions investigated with all three radiations. However, the differences are within just 9%, and their significance is not clear. A fit of the $F_a(G_\perp)$ data reported in [2] yielded $R_c = 7.82$ Å. For our as-quenched Au-substituted alloys, the R_c-values are higher, which is to be attributed to changes in the hypersphere shapes (or weights), due to the Au contribution. The R_c-values measured for the $x = 0$ and 1 samples with Cu Kα and with synchrotron radiation differed by less than 4%.
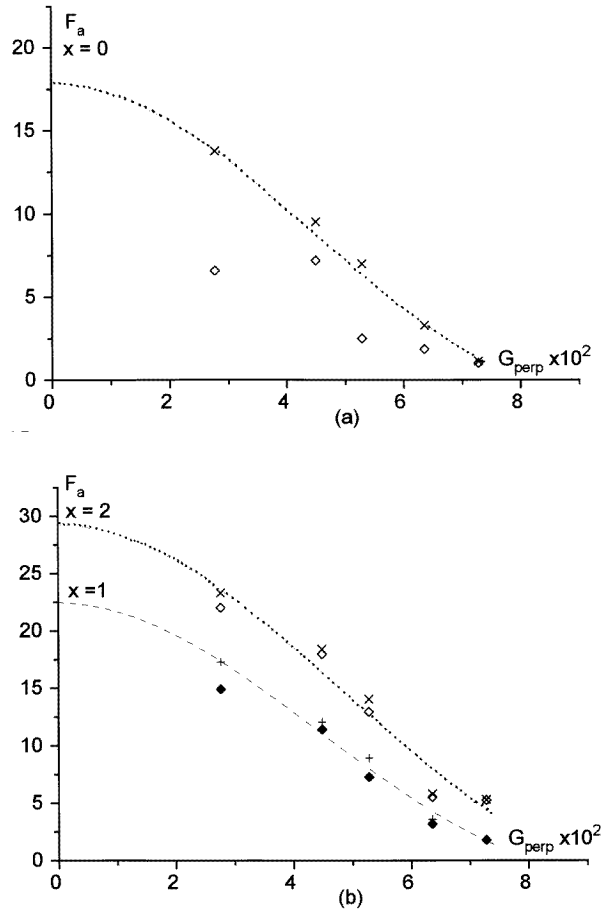
Figure 2. Experimental structure factors F_a of icosahedral lines versus $G_\perp$ (for different Au contents x); synchrotron radiation data with $\lambda = 1.50$ Å ($x = 2, 5, 7$) and XRD data ($x = 0, 1$). $\diamond, \blacklozenge$: uncorrected; $\times, +$: corrected with a Debye–Waller factor. The F_a-values are multiplied by an arbitrary scale factor.

Table 2. The average hypersphere radius R_c for λ_{Au}, λ_n, and λ_{Cu}; synchrotron radiation data, if not otherwise stated.

x	R_c^{Au}	R_c^n	R_c^{Cu}
0	—	8.78[a]	—
1	—	8.64[a]	—
2	8.31	8.71	8.74
5	8.39	8.63	8.50
7	8.48	8.83	7.95
i-Al$_{63}$Cu$_{25}$Fe$_{12}$	—	7.82[b]	—

[a] Cu Kα XRD data.
[b] Data from [2].

5.4. Calculated structure factors

Having found average $S_k^{exp}(G_\perp)$ functions describing the $F_k(G_\perp)$ experimental dependences, we can now calculate F_k-values for different values of $G_\parallel$, compositions x, and atom
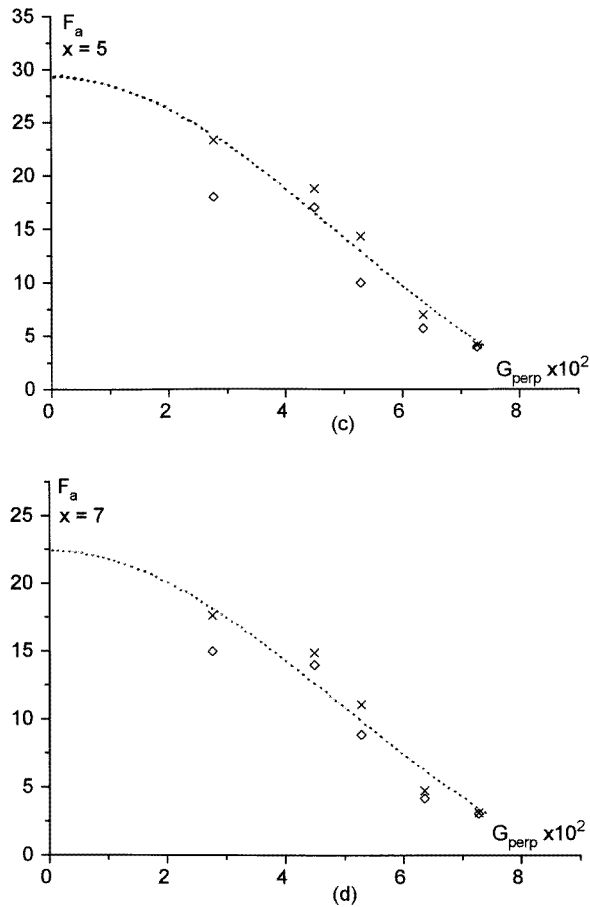
Figure 2. (Continued)

distributions. We can write, using equation (6),

$$
F_k(G_\parallel, G_\perp) = \left| \frac{S_k^{\exp}(G_\perp)}{S_k^{\exp}(G_\perp \to 0)} \sum_j \tilde{\mu}_j \sum_i c_i^j f_i(G_\parallel) \right|
\tag{7}
$$

where all quantities are known.

5.5. Derivation of experimental structure factors

Experimental structure factors F_k were derived from integrated intensities, measured with synchrotron radiation ($\lambda_n = 1.50$ Å). Lorenz-polarization corrections were applied, as are suitable for diffractometry on polycrystalline samples. The multiplicities $m(N, M)$ of the icosahedral lines were as those of the similar i-AlPdMn structure [13]. The atomic scattering amplitudes were calculated using nine-parameter polynomial approximations [14]. The experimental intensity data were also adjusted by applying a Debye–Waller correction, using an average B-factor derived from the $F_k(G_\perp)$ fit for different compositions.

We selected, for the intensity analysis, medium and strong icosahedral lines only, in order to improve the reliability. It must be recalled that the relatively high phonon/phason

disorder in our samples (see section 7) drastically reduces the number of measurable lines.

Experimental structure factor ratios F_b/F_a are good test quantities for different atomic distribution models, mainly describing the Au distribution over the icosahedral network sites. Lines of type b are sensitive, due to their 'difference' character (equations (3)), to the atom partition between $(N_1 + N_2)$ and BC_1 sites, while a-type reflections are distribution insensitive. On the other hand, using F-ratios cancels occasional unknown experimental factors affecting intensities, and that are dependent, for example, on the precise amount of substance in and geometry of the sample. In the following, use will be made of integrated intensity ratios measured with $\lambda_n = 1.50$ Å synchrotron radiation. Ratios measured with conventional equipment and Cu Kα radiation ($\lambda = 1.541\,78$ Å) are within $\pm 15\%$ of them. The choice of a lines was extended up to $G_\perp \cong 7.3 \times 10^{-2}$ Å^{-1}, including five reflections. For b-type lines, the choice also comprised five lines ($G_\perp \leqslant 6.2 \times 10^{-2}$ Å^{-1}).

5.6. Models of Au site occupation

Due to the high scattering power of Au, we expect the F_b/F_a values to be fairly sensitive to the type of site occupied by the noble metal.
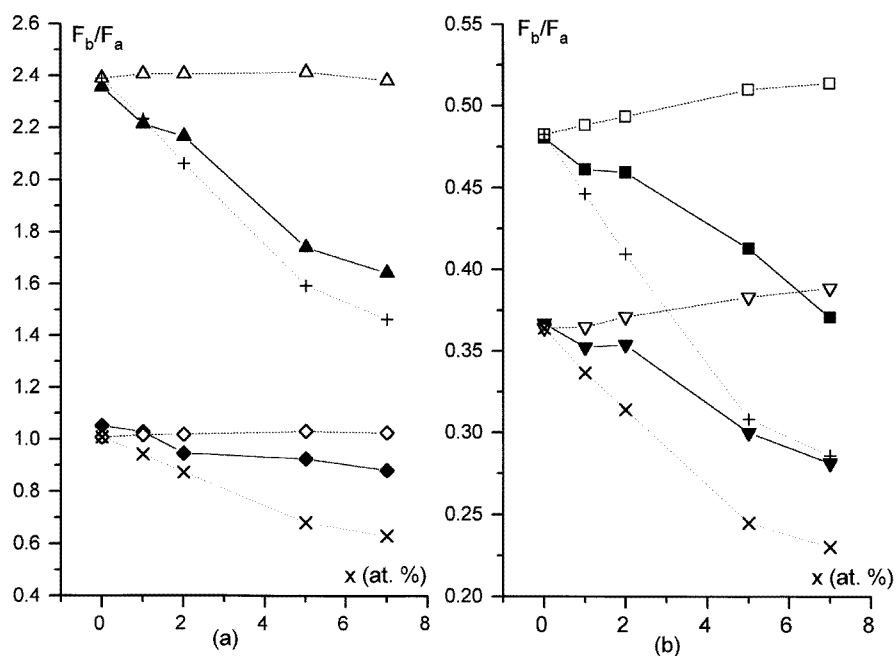
Figure 3. Experimental and calculated F_b/F_a ratios of icosahedral lines versus the Au content. (a) $(18, 29/72, 116)$ (▲: experimental; △: model I; +: model II); $(18, 29/52, 84)$ (◆: experimental; ◇: model I; ×: model II); (b) $(70, 113/52, 84)$ (■: experimental; □: model I; +: model II); $(38, 61/20, 32)$ (▼: experimental; ▽: model I; ×: model II). Synchrotron radiation data ($x = 2, 5, 7$) and XRD data ($x = 0, 1$).

Figure 3 shows the variation of several experimental F_b/F_a structure factor ratios with composition x. A decrease with Au concentration is noticed for all ratios. This behaviour is evidence for a preferential Au distribution over the network sites (in the case of a perfectly random distribution of all atoms, the intensity ratios would be composition independent).

Two simple models can be suggested for the Au distribution.

I $\Rightarrow$ Au substitutes on N_2 and/or N_1 sites, replacing Al as well as Cu, as suggested by the EDS (table 1). The two substitutions yield similar results, in view of the symmetry of the F_b-expression versus the N_1 and N_2 sites.
II $\Rightarrow$ Au substitutes integrally on BC_1 sites.

Mixed variants of these extreme models are, of course, also possible. Figure 3 compares the calculated F_b/F_a ratios with the experimental ones. Actual i-phase compositions were taken in the calculation, as derived from the EDS data (table 1). The calculated ratios could in principle be affected by the imprecision in the R_c- and B-factors which fit the $F_k(G_\perp)$ dependence. However, using the composition-dependent values $R_c(x)$ and $B(x)$ or their average causes a shift of the calculated ratios by less than 10%. These shifts do not significantly alter the slope of the F_b/F_a versus x curves. Several observations can be made on figure 3.

(i) Model I is excluded for all reflections and compositions, on the basis of the continuous decrease with x shown by the experimental ratios.
(ii) Model II is best confirmed by experiment, judging by the negative slope of the x-dependence.

Although the sign of the experimental slopes (figure 3) corresponds to model II (Au on BC_1 sites), their average magnitudes are generally less. Out of 17 F_b/F_a experimental ratios evaluated, 13 have negative slopes with magnitudes within 0.4 and 0.9 of that predicted by the model II. This observation suggests that Au is only partially placed on BC_1 sites, surrounded by aluminium configurations. The remaining Au could be located on N_1 and/or N_2 sites (a slight admixture of model I). This hypothesis is supported by the EDS data (table 1), which show that, besides Cu, Au is also substituting for some Al atoms. However, another possibility suggests itself, which can account for a fraction of Au not contributing to the icosahedral diffraction lines. Evidence from Mössbauer spectroscopy using ^{197}Au [15] revealed two Au positions, differing in their isomer shifts (IS). The high-IS configuration continuously increases with increasing Au content in the global composition. On the other hand, diffraction patterns (figure 1) show for $x = 5$ and 7 weak details which can be attributed to $AuAl_2$ lines, with lattice parameters of 5.941 and 5.950 Å respectively, as compared with 5.997 Å for pure $AuAl_2$. The high-IS Mössbauer component could then be attributed to Au in local $AuAl_2$-like configurations.

These facts suggest that, when entering Al-surrounded BC_1 (or N_2) sites, a fraction of gold shapes its local configuration in a $AuAl_2$-like way (eight Al in the corners of a cube). It is worth recalling that Cu sites of the N_2 type are surrounded by 7.5 Al neighbours [16]. The fraction of $AuAl_2$-like configurations increases with Au concentration. This tendency is to be attributed to the high stability of the $AuAl_2$ compound, due to the sp–d hybridization of the Au–Al metallic bonds (see section 8). The $AuAl_2$-like zones contribute their own diffraction peaks. Therefore, they can account for the Au 'missing' from diffracted intensities of the icosahedral phase.

Several observations point to the local character of the $AuAl_2$-type zones. First, the linewidths of this phase are about twice as large as those of the icosahedral one, showing their small coherence length. It must be stressed that SEM for samples with $x \leqslant 7$ does not reveal clear $AuAl_2$ segregations, supporting their small extent. Thus, EDS compositional data (table 1) refer to the icosahedral phase including the small $AuAl_2$-like zones. A crystallographic relationship is suggested between the $AuAl_2$ inclusions and the β- (FeAl-type) crystalline phase. The lattice parameter of the latter is about half that of $AuAl_2$ in all of

the samples investigated, causing systematic line superpositions. No extra width was found for the common lines in comparison with the others, suggesting a possible superstructure nature of the $AuAl_2$ inclusions.
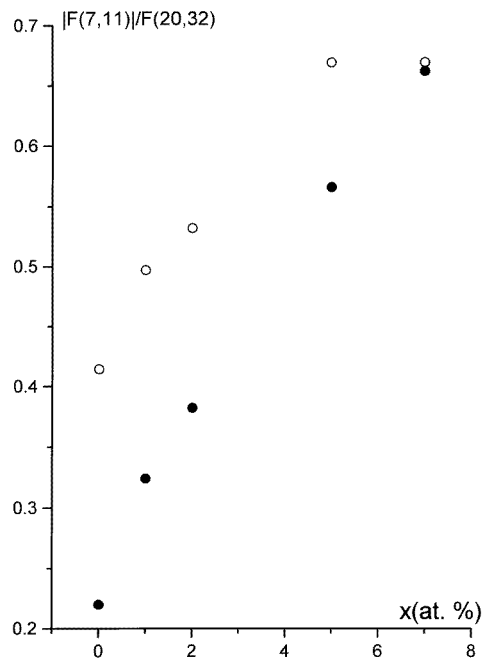

Figure 4. Experimental (●) and calculated (model II) (○) $|F(7, 11)|/F(20, 32)$ ratios versus the Au concentration x.

One of the strongest lines for $AuAl_2$ ((111), $I_{rel} = 90$) almost superposes on the icosahedral $(7, 11)$ one (the distance between centroids $\Delta(k) = 3 \times 10^{-3}$ Å at power -1). Crystalline segregations of $AuAl_2$ will therefore cause an artificial increase in the intensity of the $(7, 11)$ line, especially at high x-values. Actually, the structure factor ratios $|F(7, 11)|/F_a$ are expected to increase with x, due to the 'c'-type nature of the $(7, 11)$ line, as predicted by model II (figure 4). However, the slope of the experimental $F(7, 11)/F_a$ ratios is higher by 58 to 84% (for different a lines) than that predicted by the model. This can be considered as additional evidence that local close-packed (111) planes of the $AuAl_2$-type increasingly form when more Au is substituted in the icosahedral network. Also, linewidths consistently show larger values for the $(7, 11)$ line, confirming its composite character.

5.7. Evidence from anomalous diffraction

Additional evidence for the Au location comes from anomalous XRD data obtained with synchrotron radiation. Figure 5 shows two $|F_c|/F_a$ ratios, measured with three wavelengths: λ_n, λ_{Au}, and λ_{Cu}. It is seen that the c/a ratios steadily increase with x for all wavelengths. As shown in the preceding section, this is due both to Au substitution mainly on BC_1 sites (model II), and to very small $AuAl_2$-like zones. Measurements of several F_c/F_a ratios showed that the increase between $x = 2$ and $x = 7$ is lower by a factor of 0.7 to 0.9 for λ_{Au} than for λ_n. Values measured with λ_{Au} are also lower than those obtained with λ_{Cu}.

These effects can be explained by the real part $\Delta f'$ of the dispersion correction
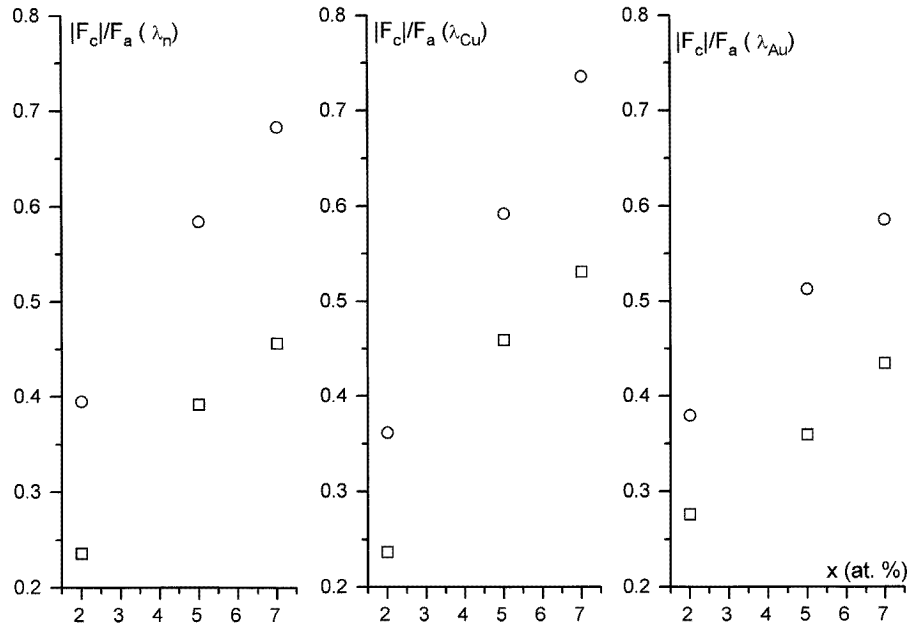
Figure 5. Experimental $|F_c|/F_a$ ratios measured with three synchrotron wavelengths: λ_n, λ_{Au}, λ_{Cu}. ○: (7, 11/20, 32); □: (7, 11/52, 84).

$(\Delta f' + i\,\Delta f'')$, which is a large negative quantity at the inflection point of an absorption edge. It follows that intensity ratios obtained with λ_{Au} are less influenced by the Au concentration and distribution. In contrast, using λ_n and λ_{Cu}, the strong scatterer Au is much more manifest. A complete evaluation of the anomalous diffraction data is in progress, using a Hönl-type algorithm for calculating complex scattering amplitudes, and will be published in detail elsewhere.
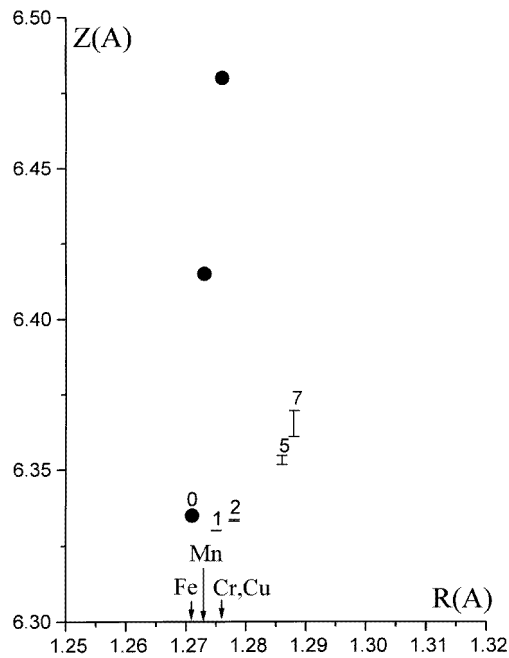
6. Parameters of the hypercubic lattice

The positions of the icosahedral lines (centroids) were used to derive the extrapolated Z-parameter of the hypercubic 6D lattice, using

$$Z_{N,M} = \frac{(N + M\tau)^{1/2}}{G_{\parallel}[2(2 + \tau)]^{1/2}}$$

where $G_{\parallel} = 2(\sin\theta)/\lambda$. The differences in Z obtained with Cohen–Wagner extrapolation functions yielding similarly small residuals are within the experimental errors.

Figure 6 shows the Z-evolution versus the average radius of non-Al atoms (data for $x = 0$ are taken from [17]). EDS compositional data were used in the calculation. Metallic radii for ligancy 12 were considered ($R_{Al} = 1.429$ Å, $R_{Fe} = 1.260$ Å, $R_{Cu} = 1.276$ Å, and $R_{Au} = 1.439$ Å). It is seen that small amounts of Au ($x = 1$ and 2) do not modify Z. However, further Au introduction on BC_1 sites forces an increasing Z-parameter. The slope is relatively mild, due to partial segregation of Au out of the icosahedral phase, into $AuAl_2$-type zones. A much steeper increase of Z was noticed for TM substitutions in Al–Cu–TM i-phases [17].

Figure 6. The hypercubic lattice parameter Z versus the average radius R of non-Al atoms. I: the Au-substituted i-Al–Cu–Fe phase. The bars cover data measured with synchrotron and Cu Kα radiation. ●: TM substitution in Al–Cu–TM i-phases (TM = Fe, Mn, Cr) (data from [17]). The experimental errors are within the symbol size.

7. Phason/phonon disorder

FWHMs of icosahedral lines (B) were used to assess the degree of random phason and phonon disorder by means of the general relationships [18, 19]

$$B^2 = AG_{\parallel}^2 + CG_{\perp}^2 + D \tag{8}$$

$$G_{\parallel} = \frac{(N + M\tau)^{1/2}}{Z[2(2+\tau)]^{1/2}} \qquad G_{\perp} = \frac{[\tau(N\tau - M)]^{1/2}}{Z[2(2+\tau)]^{1/2}} \qquad \tau = \frac{1+\sqrt{5}}{2}. \tag{9}$$

Here, A and C are parameters measuring the degree of phonon and random phason disorder, respectively, while D is inversely proportional to the icosahedral coherence length.

The linewidths were evaluated by profile matching with Voigt functions, and the parameters A, C, and D were determined by a fit to equation (8). The B-values of individual lines were weighted by their areas, thereby reducing the contribution of weak, less reliable lines. The composite line (7, 11) was not taken into account.

Fitting equation (8) to the FWHMs of the 12 most intense icosahedral lines resulted in the A- and C-values given in figure 7. The random phason and phonon disorder are seen to show no coherent variation with the Au content, if the difference between the synchrotron and sealed-source data is taken into account. We must conclude that Au substitution, as well as the presence of AuAl$_2$-like zones, induces negligible disorder in the i-AlCuFe network. By contrast, Ag substitution was found [8] to cause a steep increase of the A- and C-parameters. In the Ag system, the sample with $x = 7$ showed high A- and C-values (2.5×10^{-5} and 7.6×10^{-3}, respectively).
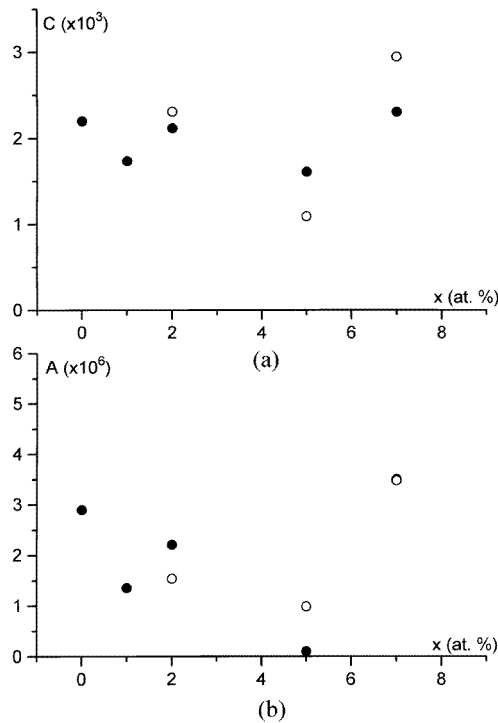
Figure 7. The parameters C and A of phason and phonon disorder versus Au concentration. ●: XRD data taken with Cu Kα radiation. ○: synchrotron radiation data ($\lambda = 1.50$ Å). For $x = 1$, only XRD data are available. For the sample with $x = 7$, the two A-values are practically coincident.

A (FWHM)^2 graph versus $G_\parallel^2$ reveals no clear increasing dependence, as would be expected if elastic strain (possibly induced by the crystalline inclusions) were the main source of line broadening.

The ratio of the first two terms in equation (8) indicates the prevalence of a certain type of disorder over the other. Using the A- and C-values (figure 7), the phason disorder contribution is larger than the phonon term by up to an order of magnitude, for all icosahedral lines. The D-values are in the range $(4.8$–$7.6) \times 10^{-6}$ Å at power -1, pointing to icosahedral coherence lengths in the region of 10^5 Å.

8. Evidence for sp–d bond hybridization in Au-substituted i-Al–Cu–Fe phases; the 'white line' in the XANES range

Hybridization of sp Al states with localized d states contributed by transition metals is a common occurrence in icosahedral phases. The presence of Fe(d)–Al(sp) hybrid bonds was predicted by self-consistent calculations of the electronic states in a model 1/1 approximant of i-Al–Cu–Fe [5]. Experimental evidence for sp–d hybridization in Al–Cu–TM i-phases and their approximants comes from exploration of occupied (bonding) and empty (antibonding) states by soft x-ray emission and absorption spectroscopies [20, 21] and from XPS. It increases the stability by widening the pseudogap at E_F and enhancing the DOS magnitude below E_F [22]. However, the problem of bond hybridization in Al-based i-phases substituted

with noble metals has not been investigated as yet.

Empty d states present in pure Fe were shown by SXAS [21] to become partly filled in i-Al–Cu–Fe. This charge transfer is to be attributed to sp–d hybridization of Fe with the surrounding Al atoms. An analysis of soft x-ray line intensities in diluted $Al_{1-x}TM_x$ alloys ($x < 0.3$) revealed [23] that the charge transfer is lower than 0.5 electrons per TM atom. On the other hand, noble metals (Au, Ag) with nearly filled d orbitals are likely to show other types of charge transfer, as a consequence of hybridization.
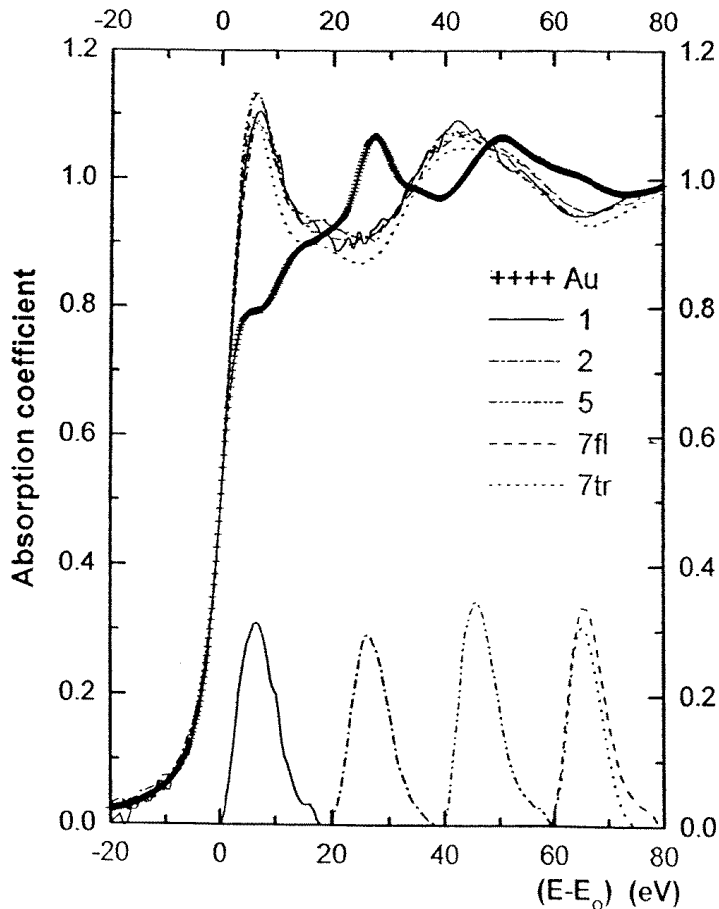
Figure 8. The XANES range of the absorption Au L_3 edge in pure Au foil and Au-substituted i-Al–Cu–Fe phases with different Au contents. White-line profiles (obtained by spectra subtraction) are shown in the lower part. Samples with $x = 1$, 2, and 5 were measured in the fluorescence mode, and the sample with $x = 7$ in both fluorescence and transmission modes.

Figure 8 shows the XANES range for i-$Al_{62}Cu_{25.5-x}Au_xFe_{12.5}$ as-quenched alloys, as compared with that of pure Au foil. The absorption data are taken around the Au L_3 edge, and are due to transitions from inner $2p_{3/2}$ levels to empty s and d states. This picture relates to the electronic states in the atomic sphere of gold. The small kink at $\cong 6$ eV above the inflexion point (Fermi level: E_F) in the pure Au foil is due to a small number ($\leqslant 0.3$) of 5d holes, present in solid gold. This detail develops into a full 'white line' (WL) in the

Au-substituted samples, pointing to antibonding states with d character being created via sp–d hybridization.

A simple model [24] and calculations supporting it [25] assume that sp charge transfer occurs from Al to Au, due to the higher electronegativity of the latter. To preserve local neutrality, an equal amount of d charge is back-transferred from Au to Al, thereby pushing some Au d states above E_F. These new empty states, created by bond hybridization, give rise to the WL absorption feature in the hybridized compounds.

The WL at the Au L_3 edge is also present in a series of crystalline Au alloys, such as $AuAl_2$ [6, 26]. The WL area was shown [27] to increase with the difference in electronegativity between Au and its ligands, and to be depressed upon alloy melting [28]. Recently, we reported [7] a study of the WL in a series of Au–B compounds with different crystalline structures, belonging to the systems Au–Ga, Au–In, Au–Sn, and Au–Ge (metastable tetragonal γ-modification). It was shown that the WL area, as a measure of charge transfer, correlates not only with the electronegativity difference, but also with the concentration of Au–B pairs in the first coordination sphere. Thereby, the study of the WL in noble-metal compounds becomes a promising new tool, which (by adequate calibration) can offer structural information about local configurations in compounds of unknown structure.

The area of the WL in Au-substituted i-Al–Cu–Fe is almost independent of the Au concentration x, taking into account the experimental precision (figure 8). This observation supports the fact that Au is surrounded by Al in both types of site that it mainly occupies (icosahedral BC_1 and cubic $AuAl_2$-type; see section 5.6).

The WL area amounts to 2.4 to 2.9 eV, and we have to compare these figures with the value of 3.6 eV measured by Jeon *et al* [27] for crystalline $AuAl_2$. The lower area found in our case could be explained by some Au substituting for Al on N_1 or N_2 sites, as is also suggested by the EDS compositions (table 1). These sites are surrounded by Cu and Fe neighbours, and are not expected to favour hybrid bonds. From the ratio 2.65/3.6 of WL areas we can estimate that, on average, 26% ($\pm 7\%$) of the Au atoms do not contribute to the white line, because they substitute at Al positions. This figure is supported by the distribution scheme derived from EDS data (table 1). Averaging the number of 'inactive' Au atoms (which substitute at Al sites), we find $(1 + 1 + 2)/(1 + 2 + 5 + 7) = 0.27$. This assumption also agrees with the lower values of F_b/F_a slopes (section 5.6). On the other hand, disorder in the Al configurations around Au could partly account for the reduction of the WL area.

9. Conclusions

Investigations of the atom positions, phason/phonon disorder, 6D lattice parameter, and absorption in the XANES range in Au-substituted icosahedral phases of the Al–Cu–Fe type can offer more than pure (quasi-) crystallographic knowledge. These structural parameters also carry information on the degree of sp–d hybridization of Au–Al pairs, mainly via the white-line effects in the XANES range. It was shown that Au preferentially substitutes for Cu on BC_1 sites, coordinated by Al. Also, a fraction of Au shapes its Al surrounding in a $AuAl_2$-like way, which is presumably best suited to strong hybrid Au–Al bonds.

We suggest that these types of analysis can shed considerable light on the crystal chemistry of icosahedral phases. They can be applied not only to well-crystallized, annealed i-phases, but also to the much more populous class of poorly organized icosahedral alloys, which form a boundary towards the amorphous metals family.

Acknowledgments

References

[1] Tsai A P, Inoue A, Yokoyama Y and Masumoto T 1990 *Metall. Trans. JIM* **31** 98
[2] Cornier-Quiquandon M, Quivy A, Lefebvre S, Elkaim E, Heger G, Katz A and Gratias D 1991 *Phys. Rev.* B **44** 2071
[3] Cornier-Quiquandon M, Bellissent R, Calvayrac Y, Cahn J M, Gratias D and Mozer B 1993 *J. Non-Cryst. Solids* **153**+**154** 10
[4] Calvayrac Y, Devaud-Rzepski J, Faudot F, Gratias D, Harmelin M, Quivy A and Bancel P A 1993 *J. Non-Cryst. Solids* **153–154** 482
[5] Trambly de Laissardière G and Fujiwara T 1994 *Phys. Rev.* B **50** 5999
[6] Jeon Y, Chen J and Croft M 1994 *Phys. Rev.* B **50** 6555
[7] Manaila R, Orton B R, Macovei D, Manciu M and Adil-Smith J 1996 *Phys. Rev.* B **53** 8164
[8] Manaila R, Macovei D, Jianu A, Popescu R, Nicula R, Zavaliche F, Devenyi A, Xie Y and Hu T 1996 *Phys. Status Solidi* b **193** 283
[9] Le Lann A 1992 *Phil. Mag.* B **66** 653
[10] Le Lann A and Devaud J 1995 *J. Physique* I **5** 129
[11] Mozer B, Cahn J W, Gratias D and Schechtman D 1986 *J. Physique Coll. Suppl.* 7 **47** C3 351
[12] Boudard M, de Boissieu M, Janot C, Heger G, Beeli C, Nissen H V, Vincent H, Ibberson R, Audier M and Dubois J M 1992 *J. Phys.: Condens. Matter* **4** 10 149
[13] Boudard M, de Boissieu M, Janot C, Dubois J M and Dong C 1991 *Phil. Mag. Lett.* **64** 197
[14] Hajdu F 1972 *Acta Crystallogr.* A **28** 250
[15] Filoti G, Manaila R, Macovei D, Jianu A, Kuncser V and Wagner F E 1997 to be published
[16] Sadoc A, Berger C and Calvayrac Y 1993 *Phil. Mag.* B **68** 475
[17] Manaila R, Manciu M, Jianu A, Popescu R and Nicula R 1995 *J. Alloys Compounds* **221** 240
[18] Horn P M, Malzfeldt W, Di Vincenzo D P, Toner J and Gambino R 1986 *Phys. Rev. Lett.* **57** 1444
[19] Manaila R, Jianu A, Popescu R and Devenyi A 1994 *J. Phys.: Condens. Matter* **6** 2307
[20] Berger C, Belin E and Mayou D 1993 *Ann. Chim. Fr.* **18** 485
[21] Sadoc A, Belin E, Dankhazi Z and Flank A M 1993 *J. Non-Cryst. Solids* **153**+**154** 338
[22] Trambly de Laissardière G, Nguyen Manh D and Mayou D 1993 *J. Non-Cryst. Solids* **153**+**154** 430
[23] Wenger A and Steinemann S 1974 *Helv. Phys. Acta* **47** 321
[24] Gelatt C D Jr, Williams A R and Moruzzi V L 1983 *Phys. Rev.* B **27** 2005
[25] Watson R E, Davenport J W and Weinert M 1987 *Phys. Rev.* B **35** 508
[26] Perez J, Qi B, Liang G, Lu F and Croft M 1988 *Phys. Rev.* B **38** 12 233
[27] Jeon Y, Qi B, Lu F and Croft M 1989 *Phys. Rev.* B **40** 1538
[28] Orton B R, Stanton C M, Gulley N A, Vorsatz D A and Manaila R 1993 *J. Non-Cryst. Solids* **156**+**158** 133